ATOMIZATION AND POWDER PROCESSING OF HIGH TEMPERATURE FERRITIC STAINLESS STEEL

Iver E. Anderson

222 Metals Development, Ames Lab. (USDOE), Iowa State Univ., Ames, IA 50011

E-mail: andersoni@ameslab.gov; Telephone: (515) 294-9791; Fax: (515) 294-8727

Joel E. Rieken

258-I Metals Development, Ames Lab. (USDOE), Iowa State Univ., Ames, IA 50011

E-mail: jrieken@iastate.edu; Telephone: (515) 294-9159; Fax: (515) 294-8727

David J. Byrd

109 Metals Development, Ames Lab. (USDOE), Iowa State Univ., Ames, IA 50011

E-mail: byrd@ameslab.gov; Telephone: (515) 294-5747; Fax: (515) 294-8727

ABSTRACT

This project pursues innovative powder processing methods and enhanced control of metal powder production by gas atomization methods and is entitled "Advanced Processing of Metallic Powders for Fossil Energy Applications." Our studies strive to enable the implementation of several emerging Fossil Energy (FE) technologies that utilize metal powders of specific size ranges and types, which are either experimental or not produced efficiently by industry. In the current work, an innovative combination of high efficiency gas atomization with modified parameters and special powder alloy designs were employed to generate precursor powder for simplified processing of high temperature Fe-based alloys for FE applications. The widely practiced approach for producing such oxide dispersion strengthened (ODS) alloys involves extensive mechanical alloying and thermal-mechanical processing and is so costly that major commercial sources for Fe-based ODS alloys are essentially lacking. In this new process (US Patent No. 7,699,905-issued in April 2010), precursor ferritic stainless steel powders were oxidized *in situ* using a unique gas atomization reaction synthesis (GARS) technique. The as-atomized powders contained an ultra thin kinetically favored (*i.e.,* Cr-enriched) surface oxide. This surface layer was used as a vehicle to carry oxygen into the alloy microstructure after powder consolidation by hot isostatic pressing (HIP) to full density. Post-HIP heat treatments were designed to drive oxygen exchange between the less stable prior particle boundary oxide and dissolved Y and other additions, e.g., Hf and Ti. The exchange reactions resulted in nano-metric Y-enriched oxide dispersoids distributed in the microstructure. Scanning electron microscopy (SEM), transmission electron microscopy (TEM), and X-ray diffraction (XRD) helped evaluate the powder product phases and evolution of the consolidated alloy microstructure. Micro-hardness testing at room temperature (RT) was used in a preliminary assessment of the strength of the alloy after heat treatment. Hardness measurements at RT also tracked the ODS alloy strengthening from dislocation sub-structure generation and annealing that was produced by incremental cold rolling up to a total of 80% reduction in area.

INTRODUCTION

Oxide dispersion strengthened (ODS) ferritic stainless steel alloys offer improved high temperature strength and creep resistance [1, 2]. For this reason, these alloys are being considered for high temperature applications within future generation thermal power systems [3-5]. The improved mechanical properties associated with ODS alloys stems from interactions between nano-metric oxide dispersoids and dislocations within the alloy microstructure [6]. The dispersoids act as pinning points that stabilize the alloy grain or sub-grain structure by impeding dislocation movement. Essentially, the effectiveness of the dispersoids to immobilize a dislocation can be thought of as a force balance between driving and dragging forces over a given dislocation line length [7]. Consequently, the resulting ODS grain or sub-grain stability is dependent on the size, distribution, and volume fraction of the dispersoid phase.

Gas atomization reaction synthesis (GARS) was employed, as an economic alternative to the traditional high cost mechanical alloying (MA) processing route, for the production of precursor powder for oxide dispersion strengthened ferritic stainless steel alloys [8, 9]. During this process, a reactive atomization gas (i.e., Ar-O_2) is used to oxidize the surface

of nascent molten alloy droplets *in situ* during primary break-up and rapid solidification of the particulate. This rapid solidification process promotes the formation of an ultra thin (t < 50nm) kinetically favored metastable Cr-enriched surface oxide layer, which is used as a vehicle to transport a prescribed amount of solid-state O into the consolidated microstructure. Elevated temperature heat-treatments are then used to drive an internal O-exchange reaction between the metastable Cr-enriched prior particle boundary (PPB) oxide and Y-enriched intermetallic compound (IMC) precipitates. This results in the formation of Y-enriched nano-metric oxide dispersoids throughout the alloy microstructure [10, 11].

In this study a select series of alloy microstructures engineered from varying powder size ranges were examined to identify the relationship between each initial as-solidified powder microstructure type and the resulting ODS microstructure. The influence of solidification rate and apparent solute segregation will be discussed as a method for controlling the ODS microstructure using this simplified GARS processing approach.

EXPERIMENTAL

The nominal atomization charge chemistry is displayed in Table 1[12]. The charge was loaded into the experimental gas atomization system and the atmosphere in the melting chamber and (connected) atomization system was evacuated with a mechanical pump to < 26.6 Pa prior to backfilling to 111 kPa of high purity Ar. Melting was performed in a yttria (Y_2O_3) painted zirconia (ZrO_2) bottom pour crucible and superheated to 1700°C. The melt pour was initiated by raising a pneumatically actuated Y_2O_3 painted alumina (Al_2O_3) stopper rod, which allowed the molten alloy to flow through a plasma sprayed Y_2O_3 lined ZrO_2 pour tube.

Table 1. Resulting CR-156 alloy composition with respect to powder particle size: CR-A) 20-53µm, CR-B) 5-20µm, and CR-C) dia. < 5µm

Alloy	Powder Size	Fe (at.%)	Cr (at.%)	Y (at.%)	Hf (at.%)	O (at.%)
CR-156YHf	Nominal	Bal.	16.00	0.31	0.12	-
CR-156YHf (CR-A)	20-53µm	Bal.	15.84	0.18	0.11	0.38
CR-156YHf (CR-B)	5-20µm	Bal.	15.84	0.18	0.11	0.76
CR-156YHf (CR-C)	Dia. < 5µm	Bal.	15.84	0.18	0.11	1.45

Upon exiting the pouring orifice, the melt was immediately impinged by the reactive atomization gas. This gas contained 0.12 vol.% O_2 mixed with high purity Ar and was directly injected through the high-pressure close-coupled atomization die at a pressure of 6.9MPa.

The resulting as-atomized powders were classified into three size divisions, measuring 20-53µm, 5-20µm, and dia. < 5µm prior to chemical or microstructural evaluation and will be referred to hereafter as CR-A, CR-B, and CR-C, respectively (see Table 1). The bulk O content for each powder range was measured using an inert gas fusion (LECO-type) analyzer, while the percentage of each metallic constituent was identified using inductively coupled plasma / mass spectroscopy (ICP/MS).

Powders representing each size division were blended with 70 vol.% Cu (dia.< 20µm), sealed in latex bags, and cold isostatically pressed (CIPed) at a pressure of 413MPa for ~60s. These cold compacts were then impregnated with epoxy and cross-sectioned for microstructural analysis.

Separately, as-atomized powders from CR-A and CR-B were placed into individual 316L stainless steel cans measuring 25.4mm in dia. x 127mm in length, while as-atomized powders from CR-C were placed into a 316L stainless steel can measuring 6.3mm in dia. x 76.2mm in length. Each can was evacuated to a pressure of ~10^{-4} Pa, outgassed at 415°C for 1hr, and electron-beam welded shut using a 316L stainless steel cap. The atomized powders then were consolidated using hot isostatic pressing (HIPing) at 700°C with 200MPa pressure for 4hrs.

The as-HIPed rods then were heat treated under vacuum (~10^{-4} Pa) at 1200°C for 2.5hrs. This heat treatment schedule had previously been reported as an effective method for forming nano-metric oxide dispersoids within similar CR-alloys [13].

Following heat treatment, sample bars were fabricated from CR-A and CR-B heat treated rods. These bars measured 13.5mm x 13.5mm x 43.6mm and 13.5mm x 8.5mm x 13.5mm, respectively. Each bar was cold rolled (at room temperature) to an ~80% reduction in area (RA) using 10% RA increments without intermediate anneals. A small section was cut from the end of each cold rolled bar following every ~20% RA stage in the progression. These sections were further segmented and annealed at 500°C or 600°C for 1hr in air.

The microhardness of each cold rolled and annealed specimen was measured using Vickers diamond pyramid indentation with a 500gm load. The average of 10 consecutive indentations for each segmented sample was plotted for each data point. Further details describing the specific characterization techniques used to evaluate these CR-alloys have been previously reported in the literature [11].

RESULTS

AS-ATOMIZED MICROSTRUCTURE

An example of the as-atomized powder morphology for each powder size division is displayed in Figure 1a-c. Most of the powders were found to be primarily spherical in shape. However, several of the larger powders (CR-A) contained satellite particles and surface dimples (see yellow arrows in Figure 1a) caused by particle-particle collisions that occur between smaller solidified powders and larger semi-solid powders. On the other hand, various smaller powders (CR-C) seemed to have solidified prior to succumbing to the effects of surface tension, resulting in a pillow-like morphology (see yellow arrows in Figure 1c). These slight variations in surface morphology provide some insight into the solidification rate experienced by individual powders.

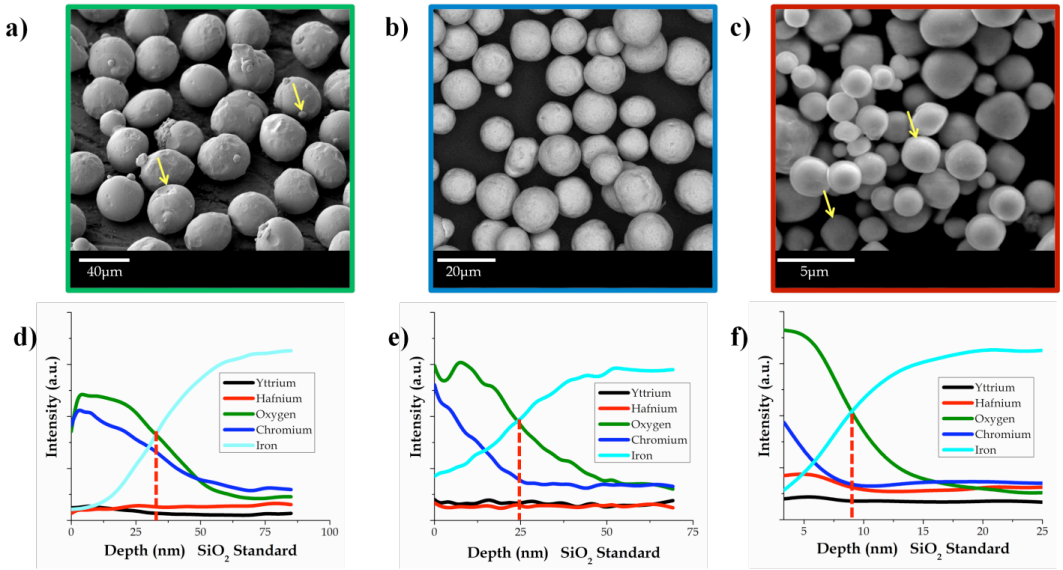

Figure 1. As-atomized powder morphology with accompanying AES depth profile: a) and d) were made from 20-53µm (CR-A), b) and e) were made from 5-20µm (CR-B), and c) and f) were made from dia. < 5µm (CR-C).

Following atomization, the resulting O content associated with the as-atomized powders was found to scale inversely with powder size (see Table 1), as surface area to volume ratio increases. Surface chemistry analysis revealed a primary enrichment of Cr (dark blue line) and O (dark green line) at the as-atomized powder surface (see Figure 1d-f) for each size division of powders, which provided evidence of Cr-enriched surface oxide phase formation during this GARS process. Furthermore, this qualitative analysis indicates that the chemistry of this surface oxide layer becomes more O-enriched compared to Cr as particle size decreases.

The thickness of the surface oxide layer was taken to be the midpoint between the maximum and minimum intensity value for O, which resulted in average thickness measurements of 33nm, 24nm, and 9nm for as-atomized powders from CR-A, CR-B, and CR-C, respectively (see vertically dashed red lines on Figure 1d-f). It also can be seen that the thickness of the oxide layer increases with particle size, suggesting that this rapid oxidation reaction is sensitive to particle cooling rate (i.e., as expected, coarser particles cool slower)

Cross-sectional analysis of the as-CIPed powders showed that CR-A and CR-B contained significant microsegregation at the as-solidified cellular boundaries, but the powders from CR-C were found to contain an apparent single phase or highly refined solidification structure (see Figure 2a-c). Additionally, EDS measurements indicated that the light contrast phase found at the cell boundaries in CR-A and CR-B was enriched in Y and Hf (see yellow arrows in Figure 2a and b), providing evidence of solute rejection upon solidification in these powders. Furthermore, no observable chemical difference was detected at (apparent) grain boundaries in CR-C (see yellow arrows in Figure 2c), indicating that significant solute trapping or nano-metric chemical segregation occurred during solidification of these ultra-fine powders.

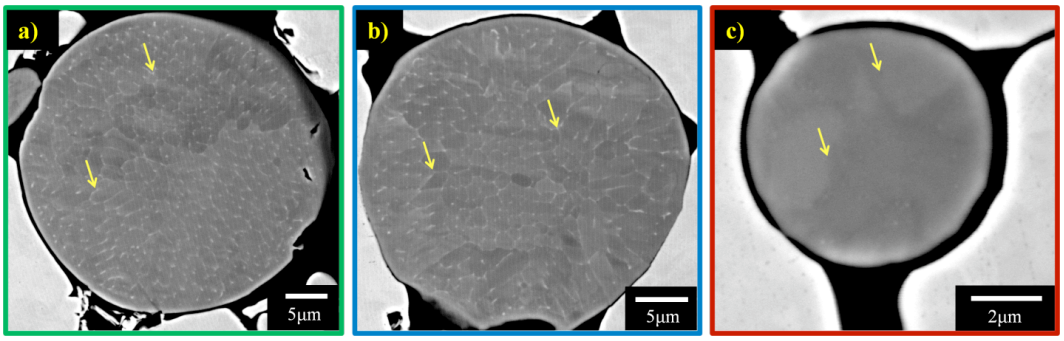

Figure 2. Cross-section SEM analysis of as-CIPed powders: a) 20-53µm (CR-A), b) 5-20µm (CR-B), and c) dia. < 5µm (CR-C).

AS-HIPED MICROSTRUCTURE

TEM was used to resolve features within the as-HIPed microstructure at a much finer size scale. The fragile nature of these low temperature consolidated TEM samples limited the area that could be observed. These results revealed the internal structure for one of the previous as-solidified cells within CR-A (see Figure 3a) highlighted by larger features along the cell boundary (see red arrow in Figure 3d) with numerous nano-metric features located near the edge of the boundary (see yellow arrow in Figure 3d). Similar nano-metric features were found to be distributed more uniformly throughout the microstructure in CR-B and CR-C (Figure 3b and c). The size of these nano-metric features in CR-C ranged between 2-6nm (see Figure 3f) with a number density of ~$4x10^{22}$ m^{-3} (number densities were estimated assuming a TEM foil thickness of 100nm).

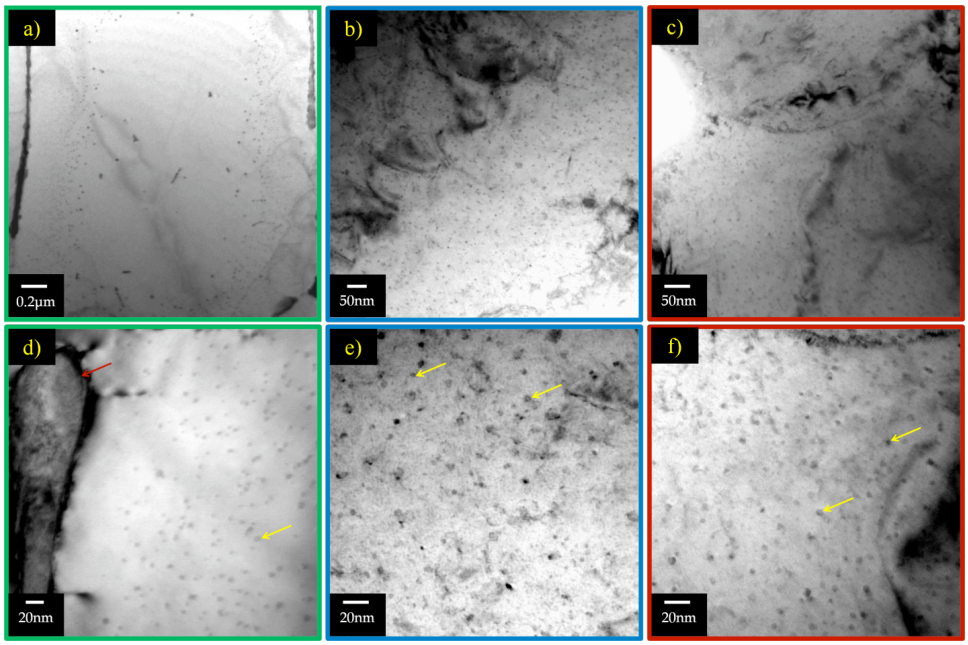

Figure 3. TEM micrographs following low temperature HIP consolidation (700°C - 200MPa - 4hrs) of the size classified powders: a) and d) with dia. of 20-53µm (CR-A), b) and e) with a dia. of 5-20µm (CR-B), and c) and f) with a dia. < 5µm (CR-C).

These features have been identified as Fe(Y,Hf), e.g., $Fe_{17}(Y,Hf)_2$ and $Fe_2(Hf,Y)$, IMC precipitates using XRD (results not shown). Additionally, APT measurements confirmed the presence of similar features within the as-atomized powders, which contain both Y and Hf with large concentrations of Fe [11]. It seems that considerable amounts of Y and Hf were rejected from solution in the α-(Fe,Cr) lattice during rapid solidification of the largest powders (CR-A) and significant solute pile-up at the as-solidified cell boundaries lead to the formation of larger elongated intermetallic precipitates. On the other hand, small amounts of solute trapping appear to have occurred near the cell boundaries in the intermediate sized (CR-B) powders, leading to the formation of some larger IMC particles and many smaller intermetallic precipitates. Notably, significant solute trapping was apparent throughout the microstructure in the finest powders (CR-C), which lead to the formation of a higher number of smaller, uniformly distributed intermetallic precipitates.

AS-REACTED MICROSTRUCTURE

Elevated temperature heat treatment (1200°C - 2.5hrs) was used to drive O exchange between the metastable Cr-enriched PPB oxide and Y-enriched IMC precipitates, promoting the formation of Y-enriched nano-metric oxide dispersoids. The resulting Y-enriched nano-metric oxide dispersoids were identified using TEM. The heat treatment resulted in the formation of ~0.5 vol.% oxide dispersoid phase throughout the CR-alloy microstructure. The distribution and size of the dispersoids varied significantly between the three powder classes (see Figure 4a-c). The dispersoids identified in CR-A seemed to be primarily distributed along previous as-solidified cell boundaries, and manifested a globular morphology, with a size range from ~20-50nm and a number density of ~$3x10^{21}m^{-3}$ (see Figure 4d). Dispersoids found in CR-B were spaced more closely, but still appeared to be arranged in a network, possibly resulting from a more refined cellular solidification structure. These dispersoids had a near spherical morphology with diameters ranging from ~5-20nm and a number density of ~$8x10^{21}m^{-3}$ (see Figure 4e). A region with a large cluster of dispersoids also was identified in CR-B (see yellow arrow in Figure 4b), which could have originated from a local region with higher Y content (e.g., an as-solidified cell boundary triple junction). The spherical dispersoids found in CR-C seemed to be distributed uniformly throughout the alloy microstructure, with a diameter of ~3-12nm and a number density of ~$3x10^{22}m^{-3}$ (see Figure 4f). Notably, the resulting dispersoids in all three powder size classes seemed to approximately mimic the spatial and size distribution of the precursor Y-enriched intermetallic precipitates. Identification of the dispersoid phases was carried out using XRD (see Figure 7 in Section 4.2 below).

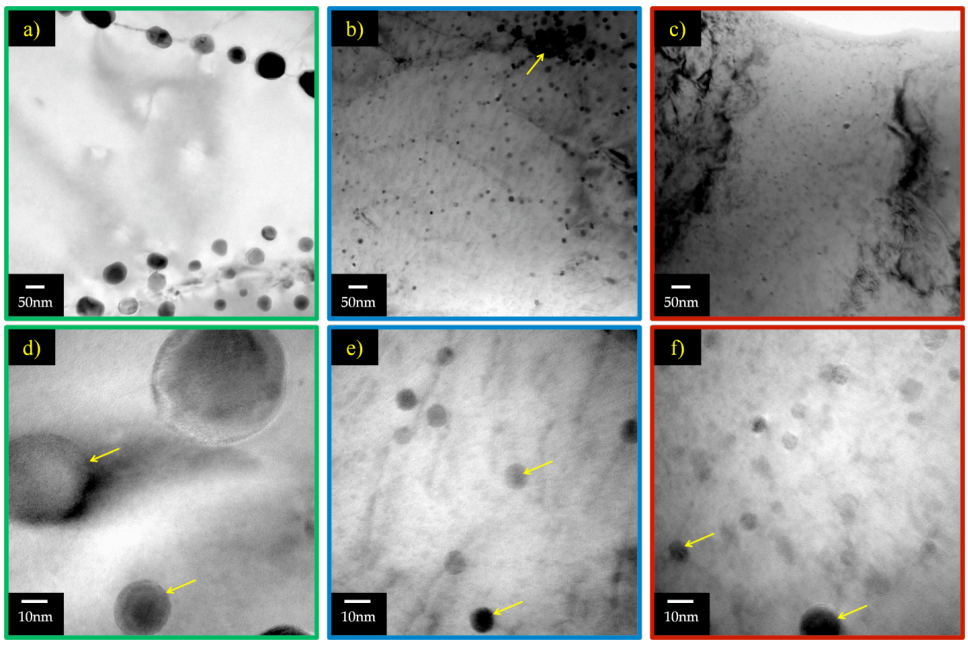

Figure 4. TEM micrographs of the heat treated (1200°C - 2.5hrs - Vac.) as-HIPed samples made from powders with: a) and d) dia. of 20-53µm (CR-A), b) and e) dia. of 5-20µm (CR-B), and c) and f) dia. < 5µm (CR-C).

MICROHARDNESS EVALUATION

Cold rolling of CR-A and CR-B in the as-heat treated condition was used to develop a fine scale dislocation substructure throughout the alloy microstructure, following the example of strengthening in MA956 [14]. The cold deformation was followed by a low temperature anneal (600°C or 500°C) to recover dislocations to dispersoid boundaries.

Microhardness measurements were used to evaluate the work hardening rate of these CR-alloys and to identify a suitable annealing temperature for a given amount of cold deformation or strain (i.e., amount of stored energy). The average microhardness data with standard deviations in the as-heat treated, as-cold rolled, and as-annealed condition are shown in Figure 5. These CR-alloy values are compared to average microhardness reported for MA956 (~275 H_v) and MA957 (~340 H_v) [15, 16]. The microhardness value used for comparison to PM2000 is a combined average (291±14 H_v) between an experimentally determined value of 312±20 H_v and a reported value of 270±8 H_v for the as-received condition [17].

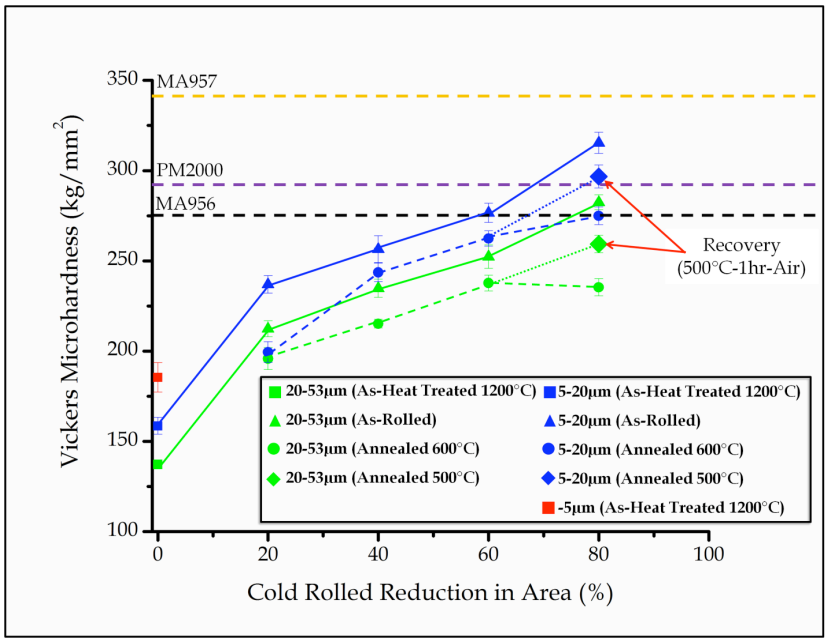

Figure 5. Resulting alloy microhardness following dispersoid formation and subsequent cold rolling and annealing trials on samples made from size classified powders identified as CR-A (green), CR-B (blue), and CR-C (red).

DISCUSSION

GARS PROCESS CONTROL

The rapid oxidation kinetics associated with this GARS reaction has been found by experiment to scale linearly with O concentration in the reactive atomization gas (Figure 6). It is believed that a consistent partial pressure of O_2 (po_2), defined by the reactive gas chemistry, is formed around the local atomization zone, thus dictating the rate of oxidation during GARS processing. Further GARS experiments will be required to better understand and model this rapid oxidation process, but early results have shown a reasonable ability to predict as-atomized O content for larger particle size classes (see horizontally dashed orange line in Figure 6). But while this empirically developed relationship has proven to work well in predicting the O content for as-atomized powders in the size range of CR-A (20-53µm) and larger, it will require further tuning to accurately predict O content in powders within the range of CR-B or CR-C (5-20µm or dia. < 5µm), which have significantly greater surface area to volume ratios.

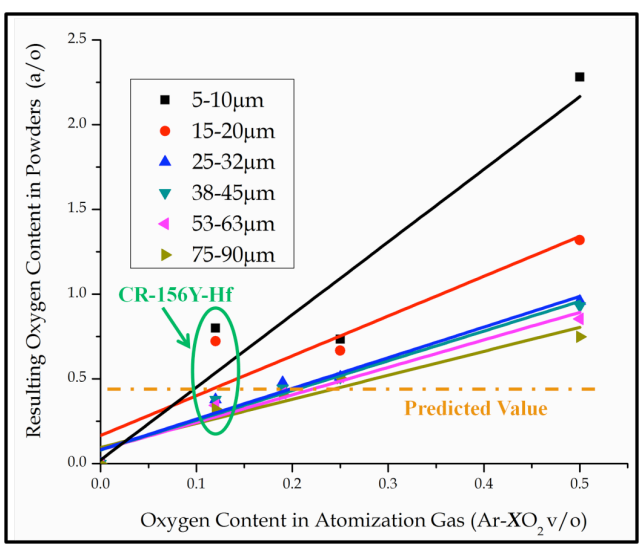

Figure 6. Resulting O content as a function of reactive atomization gas concentration for several (labeled) close size fractions.

MICROSTRUCTURAL EVOLUTION

This GARS process promoted the formation of an ultra-thin (t < 50nm) metastable Cr-enriched surface oxide layer (see Figure 1), which encases the CR-alloy powders during rapid solidification. Upon low temperature consolidation, this metastable phase was locked into position along internal PPBs. Trapping the metastable Cr-enriched oxide phase internally is thought to further reduce the oxide stability by lowering the O activity along the phase boundary, seemingly creating a near perfect vacuum for the ensuing dissociation and O exchange process. As a result, elevated temperature heat treatments were successful in dissociating this PPB oxide, allowing O to diffuse towards the interior of the powder particle driven by a concentration or chemical potential gradient. The O was subsequently consumed through internal oxidation of Fe-(Y,Hf) intermetallic precipitates, resulting in the formation of more thermodynamically stable mixed nano-metric Y-Hf-O dispersoid phases, in the case of CR-C, located throughout the alloy microstructure (see Figure 4 and Figure 7).

This type of O exchange reaction is described as diffusionless internal oxidation [18], given that the rate of reaction is controlled by the internal diffusion of only interstitial O, since both reactive metal species (i.e., Y and Hf) have limited solubility and diffusivity in the α-(Fe,Cr) matrix. In the case of CR-C the internal O exchange reaction allows for fine scale oxide dispersoid formation throughout the microstructure. More generally, internal patterns of Fe-(Y,Hf) intermetallic precipitates, which form (most likely) upon rapid solidification (Figure 3), are transformed into nano-metric oxide dispersoids. That is, the chemistry, size, and distribution of these oxide dispersoids is intrinsically linked to the precursor intermetallic chemistry, size, and distribution (see Figure 4 and Figure 7).

The oxide dispersoid chemistry was found to be influenced not only by the precursor intermetallic chemistry, but also by the initial O content in the as-atomized powders. Precursor intermetallic precipitates were found to contain both Y and Hf (see reported atom probe tomography results in reference [11]) and are believed to be either $Fe_{17}(Y,Hf)_2$ or $Fe_2(Y,Hf)$ IMC phases based on preliminary XRD results. These precursor phases were internally oxidized during elevated temperature heat treatment, resulting in the formation of mixed Y-Hf-O nano-metric oxide dispersoids (see XRD results in Figure 7). It should be noted that only CR-C contained a uniform distribution with dispersoids (dia. < 10nm) throughout the α-(Fe,Cr) matrix.

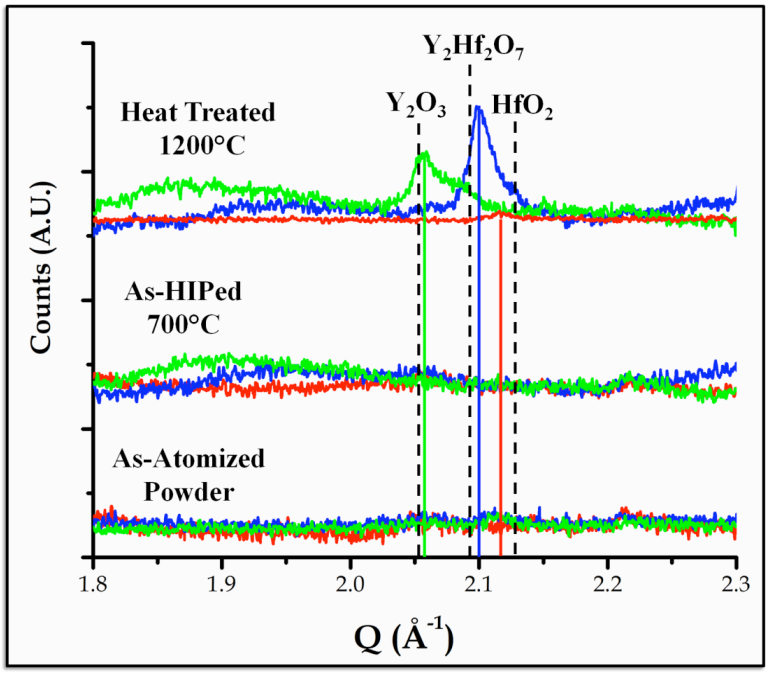

Figure 7. XRD data revealing dispersoid formation following elevated temperature heat treatment of CR-A (green trace and peak marker), CR-B (blue trace and peak marker), and CR-C (red trace and peak marker) with reference peak positions (adjacent black dashed lines) for Y_2O_3, $Y_2Hf_2O_7$, and HfO_2 [19-21].

The presence of Y, Hf, and O within the dispersoids also was confirmed using energy filtered TEM (see example in reference [13]). However, the specific dispersoid phase in each powder size class was found to contain a different crystal structure (see XRD data in Figure 7). These dispersoids seem to form as Hf-modified Y_2O_3 (CR-A), $Y_2Hf_2O_7$ (CR-B), and Y-modified HfO_2 (CR-C). This shift in crystal structure seems linked to the initial local chemistry of the precursor Fe-(Y,Hf) IMC precipitates. Additionally, the O content in the powders increases in going from CR-A to CR-C, and the

corresponding dispersoid phases reflect an increased O to Hf + Y ratio, thus, highlighting the importance of O in phase selection. Furthermore, the asymmetrical XRD peak shape or shift in peak position associated with the dispersoid phases (see displacement of dashed and solid color lines in Figure 7) is likely related to varying concentrations of Y or Hf within the modified oxide structure. It should be noted that the heat treated (1200°C) CR-C XRD specimen contained a much smaller cross-sectional area compared to CR-A and CR-B, resulting in significantly reduced counts, but still a distinct peak above background. To verify these observations of peak shifts and oxide structure differences, analogous samples from each CR-alloy will be re-examined in the near future using high-energy through-penetrating X-rays (where a significantly reduced sample size is sufficient: see example in [10]), in order to more accurately characterize the dispersoid crystal structure.

The size and distribution of the nano-metric oxide dispersoids was shown to closely mimic that of the precursor intermetallic precipitates (see Figure 3 and Figure 4). The scale of this precursor microstructure is thought to be controlled by the rapid solidification rate and cooling rate for a given powder size. The powders in CR-A (20-53μm) and CR-B (5-20μm) contained significant amounts of microsegregation, while powders in CR-C (dia. < 5μm) seemed to contain an apparent single phase or highly refined microstructure (see Figure 2). This infers that the ultra-fine (CR-C) powders were successful in solute trapping Y and Hf within the α-(Fe,Cr) lattice, by suppressing microsegregation during solidification.

Achieving such non-equilibrium microstructures is possible through the enhanced kinetics of rapid solidification. This phenomenon has been explained by Glicksman [22], through the concept of a kinetic phase diagram, based on the work of Chernov et al. [23], which illustrates how equilibrium solidus and liquid lines move together with increasing solidification velocity, thus approaching the T_0 limit [24]. Therefore, the ultra-fine (CR-C) powders must have solidified above the threshold solidification rate to suppress Y and Hf segregation.

Larger undercoolings associated with production of ultra-fine gas atomized powders supports the idea of an apparent increased solidification rate found in CR-C. These powders are capable of reaching large undercooling, due to the absence of heterogeneous nucleation sites or "motes" within each individual particle volume [25]. The concept of mote isolation, as described by Turnbull [26], indicates that the fraction of "mote" free volume can be significantly enhanced by subdividing a melt into finely dispersed particles, thus decreasing radically the probability that a given particle will contain a potent nucleation catalyst.

DISLOCATION SUBSTRUCTURE

Thermal-mechanical processing was used to develop a fine scale dislocation substructure within heat treated samples CR-A and CR-B. This procedure was adapted from previous work reported on the recovery and recrystallization of MA956 using various cold swaging and annealing treatments [14], which revealed how the balance between driving and dragging forces can influence dislocation recovery within the ODS microstructure. Furthermore, this critical balance was shown to depend strongly on the distribution of oxide particles throughout the microstructure, which controls deformation homogeneity and effective particle pinning forces [14].

The apparent work hardening rate witnessed in these CR-alloys (Figure 5) is comparable to other metal systems containing non-deforming hard particles (e.g., Cu-BeO) [27]. An initial increased hardening rate (up to ~20% RA) is thought to occur due to the formation of Orowan loops around the nano-metric oxide dispersoids, which further reduces their effective spacing, and results in large internal stresses [28]. Additionally, further deformation of these CR-alloys resulted in a noticeable decrease in work hardening rate, which is likely due to stain induced activation of secondary dislocation slip systems [29].

The heavily deformed cold rolled samples (i.e., ~80% RA) contained large amounts of stored energy, which is a large driving force for recrystallization. Subsequent annealing of these samples at 600°C seemed to provide the necessary energy for boundaries to be sufficiently mobile even when restricted by dragging forces (i.e., Zener pinning [7]) of the nano-metric oxide dispersoids, leading to partial recrystallization and more significant loss in microhardness than at lower strains associated primarily with dislocation recovery processes. On the other hand, annealing these samples at 500°C appeared to limit boundary mobility, encouraging dislocation recovery to dispersoid interfaces, resulting in the formation of a fine cellular (sub-grain) dislocation substructure throughout the CR-alloy microstructure (see Figure 8). This agrees well with the findings of Ritherdon et al. [30], which showed a threshold temperature of 570°C for preventing the occurrence of recrystallization in as-milled ODS-Fe_3Al and PM2000 powders.

As expected, the cell (sub-grain) size of these dislocation substructures was found to closely follow the distribution of nano-metric mixed Y-Hf-O dispersoids in these samples (see Figure 4). These results suggest that the dislocation substructure pattern is intrinsically linked to the original solidification structure within the as-atomized powders, i.e., this solidification structure predefines the size and distribution of the ensuing oxide dispersoids in these CR-alloys. This offers the unique possibility to engineer specific ODS microstructures through the use of selected precursor powder particles.

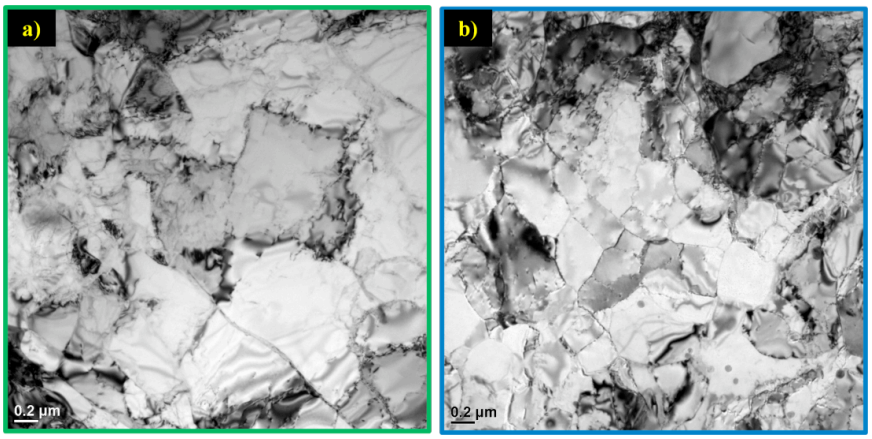

Figure 8. Dislocation substructure after HIP and annealing, followed by ~80% RA and a 1hr anneal at 500°C in air in samples made from size classified powders of: a) 20-53µm (CR-A) and b) 5-20µm (CR-B).

CONCLUSIONS

Gas atomization reaction synthesis (GARS) was used as a simplified approach to produce precursor oxide dispersion forming ferritic stainless steel powders. Mixed nano-metric Y-Hf-O dispersoids formed through solid state O exchange reactions between metastable Cr-enriched oxide and Fe-(Y,Hf) intermetallic precipitates, during elevated temperature heat treatment of these precursor powders. Resulting ODS microstructures were shown to be highly dependent on powder particle size (i.e., solidification rate). Small powders with increased amounts of solute trapping or highly refined solidification structures resulted in finer and more uniformly distributed nano-metric oxide dispersoids. Selection of powder particle size range (i.e., solidification morphology) was shown to be a viable method to control the final ODS microstructure. Thermal-mechanical processing was used to develop a fine scale dislocation substructure, which resulted in significant increases (~2X) in alloy microhardness as a direct indication of enhanced strength.

ACKNOWLEDGEMENTS

Support from the Department of Energy, Office of Fossil Energy (ARM program) through Ames Laboratory contract no. DE-AC02-07CH11358 is gratefully acknowledged. The authors also would like to thank J. Anderegg from Ames Laboratory-USDOE, and E. Fair and A. Spicher from Iowa State University for their individual contributions to this paper.

REFERENCES

[1] R.L. Klueh, J.P. Shingledecker, R.W. Swinderman, D.T. Hoelzer, "Oxide dispersion-strengthened steels: A comparison of some commercial and experimental alloys," *J. Nucl. Mater.,* vol. 341, pp. 103-114, 2005.

[2] A. Nagode, L. Kosec, B. Ule, and G. Kosec, "Review of Creep Resistant Alloys for Power Plant Applications," *Metalurgija,* vol. 50, pp. 45-48, 2011.

[3] B.K. Kad, I. Wright, G. Smith, and R. Judkins, "Optimization of Oxide Dispersion Strengthened Alloy Tubes," in *19th Annual Conference on Fossil Energy Materials*, Knoxville, TN., 2005, pp. 1-9.

[4] J.P. Hurley, "Applications for Dispersion-Strengthened Alloys in Thermal Power Systems," in *21st Annual Conference on Fossil Energy Materials*, Knoxville, TN., 2007, pp. 29-37.

[5] P. Yvon, and F. Carré, "Structural materials challenges for advanced reactor systems," *J. Nucl. Mater.,* vol. 385, pp. 217-222, 2009.

[6] A. Kelly, and R.B. Nicholson, *Strengthening Methods in Crystals*. New York, NY: John Wiley & Sons, Inc., 1971.

[7] C.S. Smith, "Grains, Phases, and Interphases: an interpretation of microstructures," *Trans. Metall. Soc. AIME,* vol. 175, pp. 15-51, 1948.

[8] I.E. Anderson, B.K. Lograsso, and T.W. Ellis, "Gas atomization synthesis of refractory or intermetallic compounds and supersaturated solid solutions," USPTO (5, 368,657), Ed. USA: Iowa State University Research Foundation, 1994.

[9] I.E. Anderson, and R.L. Terpstra, "Dispersoid Reinforced Alloy Powder and Method of Making," USPTO (7, 699,905), Ed. USA: Iowa State University Research Foundation, 2010.

[10] J.R. Rieken, I.E. Anderson, M.J. Kramer, "Microstructure Evolution of Gas-Atomized Iron-Base ODS Alloys," *Int. J. Powder Metall.,* vol. 46, pp. 17-21, 2010.

[11] J.R. Rieken, I.E. Anderson, M.J. Kramer, G.R. Odette, E. Stergar, and E. Haney, "Reactive Gas Atomization Processing for Fe-based ODS Alloys," *J. Nucl. Mater.,* vol. In Press, p. XX, 2011.

[12] Materials Preparation Center, Ames Laboratory, US DOE Basic Energy Sciences, Ames, IA, USA, available from: www.mpc.ameslab.gov.

[13] J.R. Rieken, I.E. Anderson, M.J. Kramer, "Gas Atomized Chemical Reservoir ODS Ferritic Stainless Steels," in *Advances in Powder Metallurgy & Particulate Materials*, Hollywood, Fl., 2010, pp. 112-131.

[14] M.F. Hupalo, A.F. Padilha, H.R.Z. Sandim, and A.M. Kliauga, "Cold Swaging, Recovery and Recrystallization of Oligocrystalline INCOLOY MA 956—Part II: Annealed State," *ISIJ Int.,* vol. 44, pp. 1902-1910, 2004.

[15] "Engineering Data Sheet for Incoloy® alloy MA956," Special Metals Corp. SMC-008, 2004.

[16] M.J. Alinger, G.R. Odette, and D.T. Hoelzer, "On The Role Of Alloy Composition And Processing Parameters In Nanocluster Formation And Dispersion Strengthening In Nanostructured Ferritic Alloys " DOE-ER-0313/43, Oak Ridge, TN, Report 2008.

[17] C. Capdevila, M.K. Miller, K.F. Russell, J. Chao, and J.L. Gonzalez-Carrasco, "Phase Seperation in PM 2000^{TM} Fe-base ODS alloy: Experimental study at the atomic level," *Mater. Sci. Eng.,* vol. A 490, pp. 277-288, 2008.

[18] F. Gesmundo, and B. Gleeson, "Oxidation of Multicomponent Two-Phase Alloys," *Oxid. Met.,* vol. 44, pp. 211-237, 1995.

[19] G. Kimmel, J. Zabicky, E. Goncharov, D. Mogilyanski, A. Venkert, Y. Bruckental, and Y. Yeshurun, "Formation and Characterization of Nanocrystalline Binary Oxides of Yttrium and Rare Earths Metals," *J. Alloys Compd.,* vol. 423, pp. 102-106, 2006.

[20] B.P. Mandal, N. Garg, S.M. Sharma, and A.K. Tyagi, "Preparation, XRD and Raman Spectroscopic Studies on New Compounds $RE_2Hf_2O_7$ (RE= Dy, Ho, Er, Lu, Y): Pyrochlores or Defect-Fluorite?," *J. Solid State Chem.,* vol. 179, pp. 1900-1994, 2006.

[21] D. Kim, S.H. Hyun, S.G. Kim, and M. Yashima, "Effective Ionic Radius of Y3+ Determined from Lattice Parameters of Fluorite-Type HfO2 and ZrO2 Solid Solutions," *J. Am. Ceram. Soc.,* vol. 77, pp. 597-599, 1994.

[22] M.E. Glicksman, *Principles of Solidification*. New York: Springer-Verlag New York Inc., 2010.

[23] A.A. Chernov, "Growth of Copolymer Chains and Mixed Crystals -Trial -And-Error Statistics," *Sov. Phys. Uspekhi,* vol. 13, pp. 101-128, 1970.

[24] J.W. Martin, R.D. Doherty, and B. Cantor, *Stability of microstructure in metallic systems*, second ed. Cambridge: Cambridge University Press, 1997.

[25] I.E. Anderson, and M.P. Kemppainen, "Undercooling Effects in Gas Atomized Powders," in *Annual TMS-AIME Meeting*, New Orleans, 1987, pp. 269-285.

[26] D. Turnbull, "Kinetics of Solidification of Supercooled Liquid Mercury Droplets," *J. Chem. Phys.,* vol. 20, pp. 411-424, 1952.

[27] A. Kelly, "The strengthening of metals by dispersed particles," *Proc. Roy. Soc.,* vol. A282, 63, p. 63, 1964.

[28] T. H. Courtney, *Mechanical Behavior of Materials*, second ed. Madison: McGraw-Hill, 2000.

[29] F.J. Humphreys, "The Interaction of Dislocations with Hard Particles," in *Micromechanisms of Plasticity and Fracture*, Dublin, 1983, pp. 1-37.

[30] J. Ritherdon, A.R. Jones, and I.G. Wright, "The Recovery and Recrystallisation of a Mechanically Alloyed ODS-Fe_3Al Alloy," *Mater. Sci. Forum,* vol. 360-362, pp. 217-222, 2001.